A mathematical model for the membrane electrode assembly of a bicarbonate electrolyzer

Song, Datong; Wang, Qianpu; Amirkiasar, Parisa Karimi; Jang, Darren

Publisher's version / Version de l'éditeur:
https://doi.org/10.1149/1945-7111/ad1067
Journal of The Electrochemical Society, 170, 12, 2023-12-15

Journal of The Electrochemical Society, 2023 **170** 123508

A Mathematical Model for the Membrane Electrode Assembly of a Bicarbonate Electrolyzer

Datong Song,[1,z] Qianpu Wang,[1] Parisa Karimi Amirkiasar,[2] and Darren Jang[1]

[1]*Energy, Mining, and Environment Research Centre, National Research Council Canada, Vancouver, British Columbia V6T 1W5, Canada*
[2]*Energy, Mining, and Environment Research Centre, National Research Council Canada, Mississauga, Ontario, L5K 1B4, Canada*

Bicarbonate electrolyzers are devices designed to convert CO_2 released in situ from bicarbonate ions into chemicals and fuels without an external source of CO_2 gas. A one-dimensional steady-state isothermal model is developed for the membrane electrode assembly of a bicarbonate CO_2 electrolyzer with a bipolar membrane design. The model incorporates species transport in both the anode and cathode electrodes due to convection, diffusion, and migration, and accounts for the catalyzed water splitting reaction at the interface of the anion exchange layer and the cation exchange layer of the bipolar membrane. A direct comparison of model simulations with available experimental data shows that the model can accurately simulate measured Faradaic efficiency and CO yield for all operating current densities. The model can also accurately simulate most of the polarization curve, with the only limitation being in the range dominated by mass transport. Compared to the other parameters studied in this paper, numerical results show that the performance of the bicarbonate CO_2 electrolyzer is more sensitive to both aqueous electrolyte saturation in the cathode catalyst layer and the catalyzed water splitting efficiency of the bipolar membrane.
 [DOI: 10.1149/1945-7111/ad1067]

Manuscript submitted July 19, 2023; revised manuscript received November 21, 2023. Published December 15, 2023. *This paper is part of the JES Focus Issue on Multiscale Modeling, Simulation and Design: In Honor of Ralph E. White.*

List of Symbols

Roman

a_v	Specific surface area, $m^2\ m^{-3}$
a_1, a_2, a_3	Fitting parameters for the catalyzed water splitting reaction and internal resistance
A_{elec}	Cross-section area of the flow channel, m^2
A^{A}_{OER}, A^{B}_{OER}	Pre-exponential factors of exchange current density of OER in acidic and base conditions, mA cm^{-2}
c_j	Molar concentration of species j, M or mol m^{-3}
D_j^m	Mass averaged Stefan-Maxwell diffusivity, $m^2\ s^{-1}$
D_j	Diffusion coefficient of species j, $m^2\ s^{-1}$
D_j^K	Knudsen diffusivity, $m^2\ s^{-1}$
D_{ji}	Binary diffusivity of species j and i, $m^2\ s^{-1}$
E	Electric field, V m^{-1}
$E_{a,OER}$	Apparent activation energy of OER, kJ mol^{-1}
f_w	Volume fraction of water in the AEL or CEL
F	Faraday's constant, C mol^{-1}
FE_i	Faradaic efficiency for the product i
H_i	Henry's constant for species i in water, atm M^{-1}
$\mathbf{i}_k$	Partial current density for reaction k, mA cm^{-2}
$\mathbf{i}_l$	Electrolyte current density, mA cm^{-2}
$i_{0,k}$	Exchange current density for reaction k, mA cm^{-2}
$\mathbf{i}_s$	Electrode current density, mA cm^{-2}
IEC	Ion exchange capacity, mmol g^{-1}
k_d	Dissociation rate constant of water
k_d^0	Dissociation rate constant without electric field E
k_n	Forward rate constant for homogeneous reaction n, s^{-1} or L $mol^{-1}\ s^{-1}$
k_{-n}	Backward rate constant for homogeneous reaction n
K_n	Stoichiometric equilibrium constant for the related homogeneous reaction
k_{GL,CO_2}	Gas-to–liquid mass transfer coefficient for species i, m s^{-1}
$k_{i,MT,j}$	Mass transfer coefficient of species j in phase i, m s^{-1}
L	Length, m
M_j	Molar mass of species j, g mol^{-1}
M_n	Molar mass of mixture, g mol^{-1}
n_k	Number of electrons transferred in the reaction k
n_{WD}	Number of electrons transferred per mole of H^+ in water dissociation reaction
$\mathbf{N}_{w,catalyst}$	Flux of protons/Hydroxide from the catalyzed water splitting reaction, mol $m^{-2}\ s^{-1}$
$\mathbf{N}_{i,j}$	Flux of liquid species j in phase i, mol $m^{-2}\ s^{-1}$
p	Pressure, Pa
q_l	Flow rate, L min^{-1}
r	Average pore radius of the catalyst layer, m
R	Gas constant, J $mol^{-1}\ K^{-1}$
$R_{B,j}$	Source term of species j in the homogeneous bulk reaction, mol $m^{-3}\ s^{-1}$
$R_{i,j}$	Source/sink term of species j in phase i, mol $m^{-3}\ s^{-1}$
$R_{k,j}$	Source terms of species j in reaction k, mol $m^{-3}\ s^{-1}$
R_{PT,CO_2}	Phase transfer rate of CO_2 between gas phase and dissolved phase, mol $m^{-3}\ s^{-1}$
s	Aqueous electrolyte saturation in the CL
$s_{k,j}$	Stoichiometric coefficient of species j in reaction k
$s_{j,n}$	Stoichiometric coefficient of species j in the homogeneous bulk reaction n
T	Temperature, K
u_i	Superficial velocity of phase i, m s^{-1}
U_k^0	Half-cell potential of reaction k, V
V_w	Molar volume of water, $m^3\ mol^{-3}$
V_m	Molar volume of membrane, $m^3\ mol^{-3}$
x	coordinate axis, m
x_{H^+}	Molar ratio of H^+ to fixed–charge groups in the CEL
x_w	Molar ratio of water to the sum of the water and fixed charge species in the membrane
y_j	Mole fraction of species j
z_j	Electron valency of species j

Greek

α_k	Charge-transfer coefficient for reaction k
δ_{TF}	Thin film thickness of electrolyte covering the inner surfaces of those pores that are filled with electrolyte in the CCL, m
ε	Porosity
ε^{rel}	Relative permittivity
ϕ_α	Potential of phase α, V

[z]E-mail: datong.song@nrc-cnrc.gc.ca

ϕ_s^0	Applied potential at cathode, V
$\Delta\phi_l$	Constant voltage drop at the interface of AEL|CEL, V
$\Gamma_1(\cdot)$	Bessel function of first-order
η_k	Overpotential of reaction k, V
κ_α	Permeability of phase α, m^2
λ	Membrane hydration
μ_α	Viscosity of phase α, Pa s
ρ_α	Density of phase α, g cm^{-3}
σ_s	Conductivity of solid phase, S m^{-1}
ω_j	Mass fraction of gaseous species j
Subscript	
aq	Aqueous
elec	Electode
g	Gas
GL	Gas to liquid
i or *j*	Chemical species
k	Reaction of OER, HER, or COER
l	Liquid
MT	Mass transfer
n	Homogeneous reaction
outlet	Outlet of the electrolyzer
PT	Phase transfer
sat	Saturated
TF	Thin film
w	Water
Superscript	
0	Standard state
A	Acidic conditions
B	Basic conditions
K	Knudsen
eff	Effective
m	Mass-averaged
ref	Reference state
rel	Relative
Acronyms	
ACL	Anode catalyst layer
AEL	Anion exchange layer
AEM	Anion exchange membrane
BPM	Bipolar membrane
CL	Catalyst layer
CCL	Cathode catalyst layer
CEL	Cation exchange layer
CEL	Cation exchange layer
CEM	Cation exchange membrane
CO2RR	CO_2 reduction reaction
COER	CO evolution reaction
HER	Hydrogen evolution reaction
MEA	Membrane electrode assembly
OER	Oxygen evolution reaction
TEA	Techno-economic analysis

Electrochemical conversion of CO_2 into value-added products has rapidly gained attention and made significant progress in recent decades.[1–3] Techno-economic analysis (TEA) studies have shown that CO_2 electrolyzers must operate at high current densities (>100 $mAcm^{-2}$) and low cell potential (<3 V) in order to be industrially viable.[4–6] The current performance of such systems is still low and needs further improvement to be industrially competitive. This will require not only breakthroughs in materials development to promote the CO_2 reduction reaction (CO_2RR), but also new electrode and electrolysis cell configurations to facilitate reactant transport in aqueous electrolytes.

Bicarbonate CO_2 electrolyzers are a type of CO_2 electrolyzer in which in situ generation of CO_2 molecules and direct conversion on the cathode side occur. A typical architecture of a CO_2 electrolyzer consists of an anode flow plate, a membrane electrode assembly (MEA), and a cathode flow plate. The MEA is an ion-conducting membrane sandwiched between the anode catalyst layer (ACL) and cathode catalyst layer (CCL), as shown in Fig. 1. Depending on the membrane used in its MEA, CO_2 electrolyzer configurations can be grouped into three categories[7]: cation exchange membrane (CEM)-based,[7,8] anion exchange membrane (AEM)-based,[8–11] and bipolar membrane (BPM)-based systems.[12,13] A BPM consists of an anion exchange layer (AEL) and a cation exchange layer (CEL), usually with an interfacial catalyst layer between them that promotes the dissociation/association process to maintain the supply or consumption of ionic charge carriers from either layer of the BPM. A BPM can effectively prevent ion crossover from one layer to another, which allows the use of distinct cathode and anode electrolytes in the same cell. BPMs have been successfully implemented in various electrochemical applications, such as fuel cells, flow batteries, water, or CO_2 electrolyzers, but they have not been optimized specifically for CO_2 electrolysis.[2]

Physics-based continuum modeling brings the most advanced computational techniques to simulate the reaction mechanism and transport phenomena in electrolysis systems and is a cost-effective way to explore new materials and novel designs for performance improvement. A comprehensive review of the modeling of porous electrodes for electrochemical synthesis can be found in Ref. 14. Delacourt, et al., built a model framework for a CEM-based CO_2 electrolysis on flat gold and silver electrodes and used the model to explain why a higher CO efficiency of ~90% is obtained on a gold electrode vs a silver electrode.[15,16] Weng, et al., developed a comprehensive model for a gas diffusion electrode of a CO_2 electrolyzer.[17] The model was validated using CO current density and CO Faradaic efficiency (FE_{CO}). Modeling results demonstrated that the catalyst layer wettability can significantly impact CO current density and FE_{CO}. Later, the authors extended this gas electrode model to a full MEA model for AEM-based electrolyzers by treating the anode as an interface[18] and employed the model to investigate the fundamental limitations of two MEA designs: one with gaseous feeds on both the anode and cathode sides and the other with an aqueous anode feed and a gaseous cathode feed. The model framework was further applied to a full Copper-catalyzed MEA for an AEM-based CO_2 electrolyzer to study the performance and limitations of CO_2 reduction with a Cu catalyst.[19] A 2-D model was developed for the cathode electrode of an AEM-based CO_2 electrolyzer where the catalyst layer was treated as a thin layer[11] and the model was employed to study species transport, especially CO_2 penetration depth with/without an ionomer layer between the catalyst layer and the electrolyte sub-domain. Coupled with machine learning, McCallum, et al.,[20] reported a computational model for an AEM-based MEA of a CO_2 electrolyzer to successfully identify the conditions for crossover mitigation and performance improvement.

BPM-based MEAs have many advantages compared to CEM- and AEM-based approaches,[21] including reduced species crossover, allowing the use of two different electrolytes, enabling the use of non-platinum Group Metal (PGM) materials for the anode oxygen evolution reaction (OER), and regulating pH via in situ H^+/OH^- production, among others. A downside of using BPMs compared to AEMs or CEMs is higher Ohmic losses.[2] Although mathematical modeling of ion transfer in the BPM is well-developed[22–25] and widely used in water electrolysis,[25–30] its adoption for the BPM-based MEA of CO_2 electrolyzers is still unavailable due to the numerical complexity when included in a full MEA model.

Recently, Lees, et al. developed a 1-D model for the cathode of a bicarbonate electrolyzer with a BPM design.[31] The model was used to successfully predict the trends of FE_{CO} and CO yields at the cathode electrode outlet. While this model provides a useful starting point for simulation of species transport and system performance during the electrolyzer operation, it only accounts for the cathode side of the system, and does not include the anode and the whole BPM domain. Building upon this previous work, we present here a 1-D, steady-state, isothermal model that considers species transport within the entire MEA domain, and includes the catalyzed water splitting reaction and the Wien effect. The Wien effect is the phenomenon that stronger electric fields can yield faster water dissociation rates.[32] Potential drops and pH variations through the MEA due to sharp changes in species concentrations can also be identified. Proton flux from the

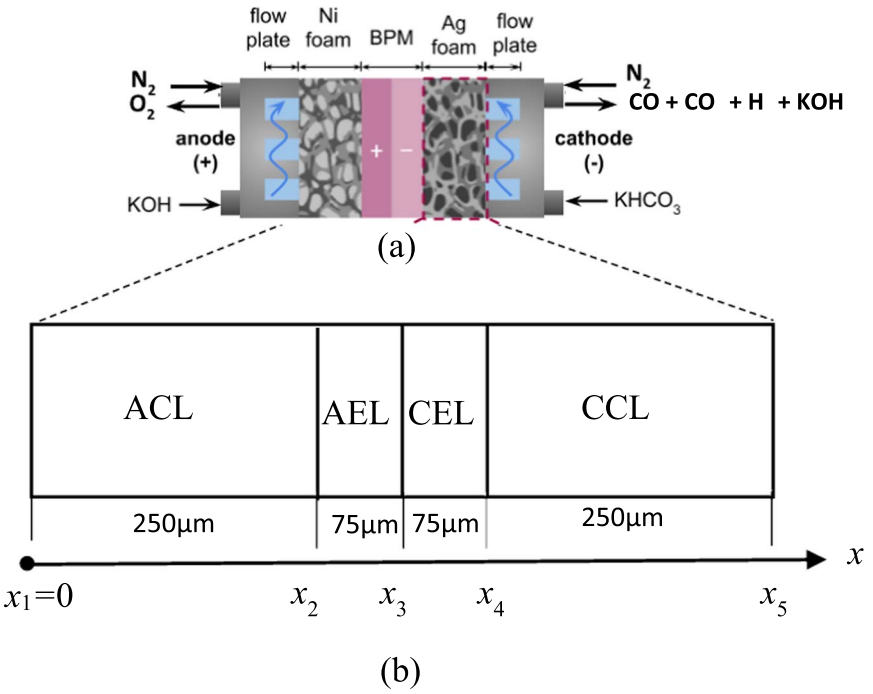

Figure 1. Schematic of a single cell of a bipolar membrane CO_2 electrolyzer.

catalyzed water splitting reaction is modeled by a quadratic function of the electrolyte current density through the AEL|CEL interface of the BPM. The potential loss due to internal resistance is also included in the boundary condition of the applied electric potential on the cathode side of the electrolyzer. The model was validated by three sets of experimental data: FE_{CO}, CO yield, and polarization curve. In the following sections, the formation of the model and its initial values and boundary conditions are presented along with a detailed discussion on the impact of MEA parameters such as porosity, saturation, etc on the performance of the modeled electrolyzer.

Model Development

The MEA of a bicarbonate electrolyzer contains a nickel foam anode, a silver foam cathode, and a BPM, as Fig. 1a.[31] The nickel foam anode is marked as an ACL while the silver foam cathode as a CCL, shown in Fig. 1b. The source of the nitrogen is the result of the purge process after each test. Gaseous reaction products formed at the cathode were delivered to the sample loop of a gas chromatograph (GC) using a stream of N_2 gas that was swept through the headspace of the 3 M $KHCO_3$ reservoir. A more detailed system operating diagram and different phase domains can be found in Refs. 12, 13, 31.

The model is developed based on the following assumptions:

- All domains are considered isothermal.
- Electrolyte flow is incompressible.
- Porous electrodes and the BPM are isotropic.
- The aqueous electrolyte saturations in both the ACL and CCL are assumed constant. Here the electrolyte saturation means the electrode saturation by an electrolyte.
- Gaseous species transport exists only in the ACL and CCL, not in the AEL and CEL. AEL and CEL are hydrophilic materials and the liquid supply (water at the AEL|CEL interface, anolyte, and catholyte) makes both AEL and CEL swell. In addition, the experiment[13] shows that the CO_2 gas bubbles accumulated at the interface of CEL|CCL and transported out through the CCL.
- The catalyst thin film between the AEL and CEL of the BPM is to enhance the water splitting reaction and is considered as an interface.
- Dissolved CO, H_2, N_2, and O_2 in electrolyte are neglected due to their limited solubility.
- Bubbling induced convection in the liquid phase of both ACL and CCL is neglected.

Reactions.—In the ACL, the OER occurs in both acidic and basic environments,[18]

$$2H_2O \rightarrow O_2 + 4H^+ + 4e^- \quad [1]$$

$$4OH^- \rightarrow O_2 + 2H_2O + 4e^- \quad [2]$$

In the CCL, CO_2 reduction reaction (CO_2RR),

$$CO_2(aq) + H_2O + 2e^- \rightarrow CO + 2OH^- \quad [3]$$

Similar to the OER, the H_2 evolution reaction (HER) in the CCL occurs in both acidic and basic environments,

$$2H^+ + 2e^- \rightarrow H_2 \quad [4]$$

$$2H_2O + 2e^- \rightarrow H_2 + 2OH^- \quad [5]$$

The following acid/base homogeneous bulk reactions occur in both the CCL and CEL,

$$CO_2(aq) + H_2O \underset{k_{-1}}{\overset{k_1}{\rightleftarrows}} H^+ + HCO_3^-, \quad K_1 = 10^{-6.37} \quad [6]$$

$$HCO_3^- \underset{k_{-2}}{\overset{k_2}{\rightleftarrows}} H^+ + CO_3^{2-}, \quad K_2 = 10^{-10.32}\text{M} \quad [7]$$

$$CO_2(aq) + OH^- \underset{k_{-3}}{\overset{k_3}{\rightleftarrows}} HCO_3^-, \quad K_3 = K_1/K_w \quad [8]$$

$$HCO_3^- + OH^- \underset{k_{-4}}{\overset{k_4}{\rightleftarrows}} H_2O + CO_3^{2-}, \quad K_4 = K_2/K_w \quad [9]$$

The non-catalyzed water splitting reaction takes place in the whole domain (ACL, AEL, CEL, and CCL),

$$H_2O \underset{k_{-w}}{\overset{k_w}{\rightleftarrows}} H^+ + OH^-, \quad K_w = 10^{-14}M^2 \qquad [10]$$

The catalyzed water splitting reaction is the same as Eq. 10 but has a different dissociation rate, and only occurs at the AEL|CEL interface of the BPM. Protons produced from the catalyzed water splitting reaction flow only into the CEL and the produced hydroxide ions flow only into the AEL.

Mass transport in the gas phase.—There are two gaseous species, O_2 and N_2, in the ACL and four gaseous species in the CCL, CO_2(g), H_2, CO, and N_2. All the electrochemical reactions (Eqs. 1 ∼ 5 and homogeneous bulk reactions (Eqs. 6 ∼ 10) are assumed to take place in the liquid phase of the corresponding electrode. Due to their low solubilities, the dissolved O_2, H_2, and CO in the liquid phase are neglected. Therefore, the source terms of O_2, H_2, and CO are the production rates of the corresponding charge transfer reaction.

The governing equation of mass conservation for the gas phase species in the electrodes of a CO_2 electrolyzer is given by

$$\nabla \cdot \mathbf{N}_{g,j} = R_{g,j} \qquad [11]$$

where g denotes the gas phase, j represents the gas phase species, i.e., $j = O_2$ and N_2 in ACL, $j = CO_2$(g), H_2, CO and N_2 in CCL, $\mathbf{N}_{g,j}$ is the mass flux of gaseous species j, and $R_{g,j}$ is the source/sink term of gaseous species j.

The mass flux, $\mathbf{N}_{g,j}$, is given by,

$$\mathbf{N}_{g,j} = -\rho_g D_j^{\text{eff}} \nabla \omega_j - \rho_g D_j^{\text{eff}} \omega_j \frac{\nabla M_n}{M_n} + \rho_g \mathbf{u}_g \qquad [12]$$

$$\sum_j \omega_j = 1 \qquad [13]$$

where ω_j is the mass fraction of species j, ρ_g and ρ_j are the mass density of the gaseous mixture and gaseous species j, respectively, D_j^{eff} is the effective diffusion coefficient of species j, M_n is the average molar mass of the gaseous mixture, and $\mathbf{u}_g$ is the velocity of the gaseous mixture.

$$M_n = \left(\sum_j \frac{\omega_j}{M_j} \right)^{-1} \qquad [14]$$

here M_j is the molar mass of gaseous species $j = O_2$ and N_2 for the anode and $j = CO_2$, H_2, CO, and N_2 for the cathode.

The density of the gas mixture can be estimated by ideal gas law as,

$$\rho_g = \frac{p_g}{RT} M_n \qquad [15]$$

where p_g is the total gas pressure of the gaseous mixture, R is the universal gas constant, and T is the temperature.

The effective diffusion coefficient of gaseous species j, D_j^{eff}, is estimated from the Bruggeman equation,

$$D_j^{\text{eff}} = (\varepsilon)^{3/2} D_j \qquad [16]$$

where ε is the volume fraction of the gaseous phase in the anode or the cathode electrode, and D_j is the bulk diffusion coefficient of species j.

$$\varepsilon = \varepsilon^0 (1 - s) \qquad [17]$$

$$D_j = \left(\frac{1}{D_j^{\text{m}}} + \frac{1}{D_j^{\text{K}}} \right)^{-1} \qquad [18]$$

where ε^0 and s are the porosity and aqueous electrolyte saturation of the anode or the cathode electrode. The mass averaged Stefan-Maxwell diffusivity, D_j^{m}, and Knudsen diffusivity, D_j^{K}, are calculated by,

$$D_j^{\text{m}} = \frac{1 - \omega_j}{\sum_{i \neq j} \frac{\omega_i M_n}{M_i D_{ji}}} \qquad [19]$$

and

$$D_j^{\text{K}} = \frac{2r}{3} \sqrt{\frac{8RT}{\pi M_j}} \qquad [20]$$

respectively. Here D_{ji} is the binary diffusivity of species j and i, r is the average pore radius in the anode or the cathode electrode.

The gas mixture velocity in Eq. 12 is determined by Darcy's law,

$$\mathbf{u}_g = -\frac{\kappa_g^{\text{eff}}}{\mu_g} \nabla p_g \qquad [21]$$

here μ_g is the viscosity of the gaseous mixture in the corresponding electrode, and κ_g^{eff} is the effective permeability of the gas phase in the electrode and can be estimated as,

$$\kappa_g^{\text{eff}} = \kappa_{\text{sat}} \kappa_g^{\text{rel}} \qquad [22]$$

where κ_{sat} is the saturated permeability and κ_g^{rel} is the relative permeability of the gas phase. κ_{sat} is given by Carman-Kozeny equation as,[33]

$$\kappa_{\text{sat}} = \kappa_{\text{sat}}^0 \frac{(\varepsilon^0)^3}{(1 - \varepsilon^0)^2} \qquad [23]$$

and κ_g^{rel} is calculated by,

$$\kappa_g^{\text{rel}} = (1 - s)^3 \qquad [24]$$

Here κ_{sat}^0 is the bulk saturated permeability of the related electrode.

The viscosity of the gas mixture in Eq. 21 can be calculated by,

$$\mu_g = \frac{\sum_j \omega_j \mu_j / \sqrt{M_j}}{\sum_j \omega_j / \sqrt{M_j}} \qquad [25]$$

where μ_j is the viscosity of gaseous species j.

The source/sink terms of gaseous species j, $R_{g,j}$, in Eq. 11 are listed in Table I.

The source terms of O_2 in reaction OER, CO in reaction COER, and H_2 in reaction HER are,

$$R_{\text{OER},O_2} = -M_{O_2} \frac{s_{\text{OER},O_2} a_v \mathbf{i}_{\text{OER}}}{n_{\text{OER}} F} \qquad [26]$$

$$R_{\text{COER,CO}} = -M_{\text{CO}} \frac{s_{\text{COER,CO}} a_v \mathbf{i}_{\text{COER}}}{n_{\text{COER}} F} \qquad [27]$$

Table I. Source/sink terms of gaseous species in the mass conservation Eq. 11.

Source term ($kgm^{-3}s^{-1}$)	ACL	CCL
R_{O_2}	R_{OER,O_2}	
R_{N_2}	0	0
R_{H_2}		R_{HER,H_2}
R_{CO}		$R_{COER,CO}$
$R_{CO_2(g)}$		$-R_{PT,CO_2}$

and

$$R_{HER,H_2} = -M_{H_2}\frac{s_{HER,H_2}a_v\mathbf{i}_{HER}}{n_{HER}F} \quad [28]$$

respectively. Where $s_{k,j}$ is the stoichiometric coefficient of species j in reaction k (negative for reactants and positive for products), a_v is the active surface area, F is Faraday's constant, n_k is the number of electrons transferred in reaction k, and $\mathbf{i}_k$ is the current densities of reaction k.

$$\mathbf{i}_{OER} = -i^{A}_{0,OER}\exp\left(-\frac{\alpha^{A}_{OER}F}{RT}\eta_{OER}\right) - i^{B}_{0,OER}\left(\frac{c_{OH^-}}{c^{ref}_{OH^-}}\right)\exp\left(-\frac{\alpha^{B}_{OER}F}{RT}\eta_{OER}\right) \quad [29]$$

$$\mathbf{i}_{COER} = -i_{0,COER}\left(\frac{c_{CO_2(l)}}{c^{ref}_{CO_2(l)}}\right)\exp\left(-\frac{\alpha_{COER}F}{RT}\eta_{COER}\right) \quad [30]$$

$$\mathbf{i}_{HER} = -i^{A}_{0,HER}\left(\frac{c_{H^+}}{c^{ref}_{H^+}}\right)\exp\left(-\frac{\alpha^{A}_{HER}F}{RT}\eta_{HER}\right) - i^{B}_{0,HER}\exp\left(-\frac{\alpha^{B}_{HER}F}{RT}\eta_{HER}\right) \quad [31]$$

where $i^{A}_{0,OER}$, $i^{B}_{0,OER}$, $i_{0,COER}$, $i^{A}_{0,HER}$ and $i^{B}_{0,HER}$ are the exchange current densities of acidic OER, basic OER, COER, acidic HER and basic HER, respectively, c_j and c^{ref}_j are the concentration and reference concentrations of species j ($j = OH^-$, CO_2(aq) and H^+), α^{A}_{OER}, α^{B}_{OER}, α_{COER}, α^{A}_{HER} and α^{B}_{HER} are the transfer coefficients of acidic OER, basic OER, COER, acidic HER and basic HER, respectively, and η_{OER}, η_{COER} and η_{HER} are the surface overpotentials of OER, COER and HER, respectively.

$$\eta_{OER} = \phi_s - \phi_l - \left(U^0_{OER} - \frac{2.303RT}{F}pH\right) \quad [32]$$

$$\eta_{COER} = \phi_s - \phi_l - \left(U^0_{COER} - \frac{2.303RT}{F}pH\right) \quad [33]$$

$$\eta_{HER} = \phi_s - \phi_l - \left(U^0_{HER} - \frac{2.303RT}{F}pH\right) \quad [34]$$

where ϕ_s and ϕ_l are the potentials of solid and liquid phases, respectively, U^0_{OER}, U^0_{COER} and U^0_{HER} are the standard reduction potentials of OER, COER, and HER, respectively.

The exchange current densities of acidic OER, basic OER are given by[18]

$$i^{A}_{0,OER} = A^{A}_{OER}\exp\left(-\frac{E_{a,OER}}{RT}\right) \quad [35]$$

$$i^{B}_{0,OER} = A^{B}_{OER}\exp\left(-\frac{E_{a,OER}}{RT}\right) \quad [36]$$

where $E_{a,OER}$(kJ mol^{-1}) is the apparent activation energy of OER and is pH-dependent,

$$E_{a,OER} = 11 + 1 \times pH \quad [37]$$

$$pH = -\log(c_{H^+}) \quad [38]$$

with the unit of c_{H^+} is ML^{-1}.

The phase transfer rate of CO_2 between gas phase and dissolved phase in the CCL is estimated by,[17]

$$R_{PT,CO_2} = a_v k_{GL,CO_2}M_{CO_2}(H_{CO_2}p_g y_{CO_2} - c_{CO_2,l}) \quad [39]$$

where k_{GL,CO_2} is the gas-to-liquid mass transfer coefficient of CO_2, H_{CO_2} is Henry's constant of CO_2, y_{CO_2} is the mole fraction of CO_2, and $c_{CO_2,l}$ is the dissolved CO_2 concentration in the CCL. $R_{PT,CO_2} < 0$ indicates that CO_2 transfers from the liquid phase into the gas phase while $R_{PT,CO_2} > 0$ means that CO_2 changes from the gas phase to the liquid phase.

The active surface area in the CCL is corrected by its aqueous electrolyte saturation as,

$$a_v = a^0_v s \quad [40]$$

where a^0_v is the specific interfacial area of CCL.

The monotonous correction of active reaction surface on electrolyte saturation, Eq. 40, is based on the understanding that only those catalyst particles in contact with liquid electrolyte are active.[17] So far, there is no better way to mathematically relate the active surface area to liquid saturation and it needs to be investigated in the future.

The gas-to-liquid mass transfer coefficient of CO_2 is given by,

$$k_{GL,CO_2} = \frac{D_{CO_2(l)}}{\delta_{TF}} \quad [41]$$

where $D_{CO_2(l)}$ is the diffusion coefficient of CO_2 in the liquid phase, and δ_{TF} is the thickness of the thin film of electrolyte covering the inner surfaces of those pores that are filled with electrolyte in the CCL.

$$\delta_{TF} = r(1 - \sqrt{1 - s}) \quad [42]$$

The Henry's constant of CO_2, H_{CO_2}, can be estimated by,[18]

$$H_{CO_2} = 34 \times \exp\left(2400 \times \left(\frac{1}{T[K]} - \frac{1}{298}\right)\right) \quad [43]$$

with the unit of mol m^{-3} atm^{-1}.

Mass transport in the liquid phase.—In the CEL and CCL, the liquid phase species are CO_2(aq), K^+, H^+, OH^-, HCO_3^-, CO_3^{2-}, and H_2O, while in the AEL and ACL, the liquid phase species are K^+, H^+, OH^-, and H_2O. The water concentration is assumed to be constant so the governing equation for water is omitted.

The governing equation of mass conservation for each liquid phase species of the electrolyzer is

$$\nabla\cdot\mathbf{N}_{l,j} = R_{l,j} \quad [44]$$

where l denotes liquid phase, j represents the liquid phase species in the anode or cathode electrode, i.e., $j = K^+$, H^+ and OH^- in the anode electrode, $j = CO_2(l)$, K^+, H^+, OH^-, HCO_3^-, and CO_3^{2-} in the cathode electrode, $\mathbf{N}_{l,j}$ is the molar flux of liquid species j, and $R_{l,j}$ is the source/sink term of liquid species j.

The flux of species j in Eq. 44 consists of diffusion, migration, and convection terms, and is defined by the Nernst-Plank equation,

$$\mathbf{N}_{l,j} = -D_j^{\text{eff}}\nabla c_j - z_j c_j D_j^{\text{eff}}\frac{F}{RT}\nabla\phi_l + \mathbf{u}_l c_j$$
$$\mathbf{i}_l = F\sum_j z_j \mathbf{N}_{l,j} \quad [45]$$

where D_j^{eff} is the effective diffusion coefficient of species j, c_j is the molar concentration of species j, z_j is the charge number, ϕ_l is the ionic potential in the liquid phase, and $\mathbf{u}_l$ is the superficial velocity vector of the liquid phase.

The effective diffusion coefficient of species j in the ACL or CCL is estimated by Bruggemann equation as,

$$D_j^{\text{eff}} = (\varepsilon^0 s)^{1.5} D_j \quad [46]$$

where D_j is the bulk diffusion coefficient of species j in the liquid phase of ACL or CCL.

The effective diffusion coefficient of species j in the AEL or CEL of the BPM is calculated as,[22,31,34]

$$D_j^{\text{eff}} = \frac{f_w}{x_w} D_j \quad [47]$$

where f_w and x_w are the volume fraction and mole fraction of water in the AEL or CEL, respectively, and they both are functions of the membrane hydration (λ),

$$f_w = \frac{\lambda V_w}{\lambda V_w + V_m} \quad [48]$$

and

$$x_w = \frac{\lambda}{\lambda + 1} \quad [49]$$

Where λ is the membrane hydration, V_w and V_m are the molar volumes of water and the membrane phase, respectively.

A linear dependence of the membrane hydration on the molar ratio of protons in the CEL (hydroxide ions in the AEL) to fixed-charge groups in the membrane is assumed,[22]

$$\lambda = \begin{cases} \lambda_{x_{H^+=0}} + x_{H^+}\lambda_{x_{H^+=1}} & \text{in the CEM} \\ \lambda_{x_{OH^-=0}} + x_{OH^-}\lambda_{x_{OH^-=1}} & \text{in the AEM} \end{cases} \quad [50]$$

where $\lambda_{x_{H^+=0}} = \lambda_{x_{OH^+=0}} = 6$ and $\lambda_{x_{H^+=1}} = \lambda_{x_{OH^+=1}} = 9$ are hydration values fit to experimental BPM data collected for a salt solution and deionized water, respectively.

The superficial velocity vector in Eq. 45 is calculated by Darcy's law,

$$\mathbf{u}_l = -\frac{\kappa_l^{\text{eff}}}{\mu_l}\nabla p_l \quad [51]$$

where μ_l is the dynamic viscosity of electrolyte, p_l is the liquid phase pressure, and κ_l^{eff} is the effective permeability of the liquid phase and can be determined by,

$$\kappa_l^{\text{eff}} = \kappa_{\text{sat}}\kappa_l^{\text{rel}} \quad [52]$$

where κ_l^{rel} is the relative permeability of the liquid phase in the electrode and is given by,

$$\kappa_l^{\text{rel}} = (s)^3 \quad [53]$$

The concentration of species K^+, c_{K^+}, can be obtained from the electroneutrality condition in the ACL or CCL electrolytes once the concentrations of other species are available,

$$\sum_j z_j c_j = 0 \quad [54]$$

The source/sink terms in Eq. 44, $R_{l,j}$, are listed in Table II and defined as follows.

The source terms related to the charge transfer reactions are given by,

$$R_{\text{COER},CO_2} = -M_{CO_2}\frac{s_{\text{COER},CO_2} a_v \mathbf{i}_{\text{COER}}}{n_{\text{COER}} F} \quad [55]$$

$$R_{\text{HER},H^+} = -M_{H^+}\frac{s_{\text{HER},H^+} a_v \mathbf{i}_{\text{HER}}}{n_{\text{HER}} F} \quad [56]$$

$$R_{\text{COER+HER},OH^-} = -M_{OH^-} \times \left(\frac{s_{\text{COER},OH^-} a_v \mathbf{i}_{\text{COER}}}{n_{\text{COER}} F} + \frac{s_{\text{HER},OH^-} a_v \mathbf{i}_{\text{HER}}}{n_{\text{HER}} F}\right) \quad [57]$$

The source terms related to the homogeneous bulk reactions are calculated by,[35]

$$R_{B,CO_2} = M_{CO_2}[s_{CO_2,1}(k_1 c_{CO_2,1} - k_{-1} c_{H^+} c_{HCO_3^-}) + s_{CO_2,3}(k_3 c_{CO_2,1} c_{OH^-} - k_{-3} c_{HCO_3^-})] \quad [58]$$

$$R_{B,H^+} = M_{H^+}[s_{H^+,1}(k_1 c_{CO_2,1} - k_{-1} c_{H^+} c_{HCO_3^-}) + s_{H^+,2} \times (k_2 c_{HCO_3^-} - k_{-2} c_{H^+} c_{CO_3^{2-}}) + s_{H^+,w}(k_w - k_{-w} c_{H^+} c_{OH^-})] \quad [59]$$

Table II. Source/sink terms of liquid species in the mass conservation Eq. 44.

Source term ($\text{molm}^{-3}s^{-1}$)	ACL	AEL	CEL	CCL
$R_{CO_2(l)}$			R_{B,CO_2}	$R_{\text{COER},CO_2} + R_{B,CO_2} + R_{PT,CO_2}/M_{CO_2}$
R_{K^+}	0	0	0	0
R_{H^+}	$R_{\text{OER},H^+} + R_{B,H^+}$	R_{B,H^+}	R_{B,H^+}	$R_{\text{HER},H^+} + R_{B,H^+}$
R_{OH^-}	$R_{\text{OER},OH^-} + R_{B,OH^-}$	R_{B,OH^-}	R_{B,OH^-}	$R_{\text{COER+HER},OH^-} + R_{B,OH^-}$
$R_{HCO_3^-}$			R_{B,HCO_3^-}	R_{B,HCO_3^-}
$R_{CO_3^{2-}}$			$R_{B,CO_3^{2-}}$	$R_{B,CO_3^{2-}}$

$$R_{B,OH^-} = M_{OH^-}[s_{OH^-,3}(k_3 c_{CO_2,l} c_{OH^-} - k_{-3} c_{HCO_3^-}) + s_{OH^-,4} \times (k_4 c_{HCO_3^-} c_{OH^-} - k_{-4} c_{CO_3^{2-}}) + s_{OH^-,w}(k_w - k_{-w} c_{H^+} c_{OH^-})] \quad [60]$$

$$R_{B,HCO_3^-} = M_{HCO_3^-}[s_{HCO_3^-,1}(k_1 c_{CO_2,l} - k_{-1} c_{H^+} c_{HCO_3^-}) + s_{HCO_3^-,2}(k_2 c_{HCO_3^-} - k_{-2} c_{H^+} c_{CO_3^{2-}}) + s_{HCO_3^-,3}(k_3 c_{CO_2,l} c_{OH^-} - k_{-3} c_{HCO_3^-}) + s_{HCO_3^-,4}(k_4 c_{HCO_3^-} c_{OH^-} - k_{-4} c_{CO_3^{2-}})] \quad [61]$$

$$R_{B,CO_3^{2-}} = M_{CO_3^{2-}}[s_{CO_3^{2-},2}(k_2 c_{HCO_3^-} - k_{-2} c_{H^+} c_{CO_3^{2-}}) + s_{CO_3^{2-},4}(k_4 c_{HCO_3^-} c_{OH^-} - k_{-4} c_{CO_3^{2-}})] \quad [62]$$

where $s_{j,n}$ is the stoichiometric coefficient of species j in homogeneous bulk reaction n ($s_{j,n} < 0$ for reactants and $s_{j,n} > 0$ for products), k_n and k_{-n} are the forward and reverse reaction rate constants for reaction n, respectively.

$$k_{-n} = \frac{k_n}{K_n} \quad [63]$$

where K_n is the equilibrium constant of the reaction n.

Electron transport.—The governing equations for the electron transport in the ACL and CCL are determined by Ohm's law and electroneutrality,

$$\nabla \cdot \mathbf{i}_s = -\nabla \cdot \mathbf{i}_l = \begin{cases} -a_v \mathbf{i}_{OER}, \text{ in ACL} \\ -a_v(\mathbf{i}_{COER} + \mathbf{i}_{HER}), \text{ in CCL} \end{cases} \quad [64]$$

and

$$\mathbf{i}_s = -\sigma_s^{eff} \nabla \phi_s \quad [65]$$

where $\mathbf{i}_s$ and $\mathbf{i}_l$ are the current densities in the solid and liquid phases, respectively, ϕ_s is the electronic potential in the solid phase, and σ_s^{eff} is the effective electric conductivity of the solid phase in the corresponding catalyst layer and calculated by,

$$\sigma_s^{eff} = (1 - \varepsilon^0)^{3/2} \sigma_s \quad [66]$$

where σ_s is the bulk electric conductivity of the solid phase of the corresponding catalyst layer material.

The electrolyte potential, ϕ_l, can be obtained from the Nernst-Plank equation Eq. 45.

Water splitting model in BPM.—The non-catalyzed water splitting reaction occurs in the whole MEA domain. The forward reaction rate constant of the noncatalyzed water splitting reaction Eq. 10 is given by,

$$k_w = k_d k_{-w} \quad [67]$$

here k_d is the dissociation rate constant.

Based on Onsager's weak electrolyte theory, the electric field enhances water dissociation (Second Wien Effect) which can be taken into account by setting the dissociation rate constant, k_d, as follows,[24,30]

$$\frac{k_d}{k_d^0} = \frac{\Gamma_l(\sqrt{-2b})}{\sqrt{-b}} = 1 + \frac{2^1}{1!2!} b + \frac{2^2}{2!3!} b^2 + \frac{2^3}{3!4!} b^3 + \cdots \quad [68]$$

and

$$b = 0.09636[\mathrm{K^2/mV}] \frac{|E|}{\varepsilon^{rel} T^2} \quad [69]$$

Where k_d^0 is the dissociation rate constant without electric field E, ε^{rel} is the relative permittivity, and $\Gamma_l(\cdot)$ is the first order Bessel function.

The catalyzed water splitting reaction occurs only at the AEL|CEL interface of the BPM. The dissociation rate constant for the catalyzed water splitting reaction is enhanced by the related functional groups[24,30] and can be increased up to two orders of magnitude.[36] For simplicity, it is assumed in this work that the reaction rate for the catalyzed water splitting reaction at the AEL|CEL interface is quadratic-dependent on the current density of the electrolyte phase and therefore the flux of protons or hydroxide ions from the catalyzed water splitting reaction can be estimated as,

$$\mathbf{N}_{w,catalyst} = (a_1 + a_2 \mathbf{i}_l) \frac{\mathbf{i}_l}{n_{WD} F} \quad [70]$$

where n_{WD} is the number of electrons transferred per mole of H^+ in the water dissociation reaction, a_1 and a_2 are the fitting parameters relating to the catalyzed water splitting reaction at the interface of the AEL|CEL. Note that this quadratic function for proton flux is a semi-empirical fit based on the fact that the water dissociation rate depends highly on the gradient of electric potential.

Boundary conditions and initial values.—The boundary conditions and initial values for mass transport are specified as follows.

For the mass transport in the gas phase, zero fluxes for all the gaseous species are specified at the ACL|AEL and CEL|CCL interfaces ($x = x_2$ and $x = x_4$),

$$\mathbf{N}_{g,j} = 0 \quad [71]$$

and at the anode channel|ACL and CCL|cathode channel interfaces ($x = x_1$ and $x = x_5$),[17]

$$\mathbf{N}_{g,j} = \rho_g k_{g,MT,j}(\omega_j^0 - \omega_j) \quad [72]$$

for $j = O_2$ and N_2 in ACL, and $j = CO_2(g)$, H_2, CO and N_2 in CCL, respectively. Here ρ_g is the gas phase density, ω_j^0 is the initial mass fraction of gaseous species j in the corresponding catalyst layer, $k_{g,MT,j}$ is the mass transfer coefficient of gaseous species j at the anode channel|ACL or CCL|cathode channel interfaces, and given by the Sherwood-Reynold-Schmidt correlation,

$$k_{g,MT,j} = \left(\frac{D_j}{L_{elec}}\right) \times 0.664 \times \left(\frac{\rho_g u_g L_{elec}}{\mu_g}\right)^{1/2} \times \left(\frac{\mu_g}{\rho_g D_j}\right)^{1/3} \quad [73]$$

where L_{elec} is the electrode length, μ_g and u_g are the viscosity and velocity of the gas phase.

The initial values for gas phase transport are specified as,

$$\omega_j = \omega_j^0 \quad [74]$$

Similar to Eq. 72, flux boundary conditions for the mass transport in the liquid phase at the anode channel|ACL and CCL|cathode channel interfaces ($x = x_1$ and $x = x_5$) are specified as,[17]

$$\mathbf{N}_{l,j} = k_{l,MT,j}(c_j^0 - c_j) \quad [75]$$

for $j = K^+$, H^+ and OH^- in the anode electrode, $j = CO_2(l)$, K^+, H^+, OH^-, HCO_3^-, and CO_3^{2-} in the cathode electrode, respectively. Here c_j^0 is the initial concentration of liquid species j in the corresponding electrode, $k_{l,\mathrm{MT},j}$ is the mass transfer coefficient of liquid species j at the anode channel|ACL or CCL|cathode channel interfaces, and given by the Sherwood-Reynold-Schmidt correlation,

$$k_{l,\mathrm{MT},j} = \left(\frac{D_j}{L_{\mathrm{elec}}}\right) \times 0.664 \times \left(\frac{\rho_l u_l L_{\mathrm{elec}}}{\mu_l}\right)^{1/2} \times \left(\frac{\mu_l}{\rho_l D_j}\right)^{1/3} \quad [76]$$

where μ_l and u_l are the viscosity and velocity of the liquid phase. u_l is given by,

$$u_l = \frac{q_l}{A_{elec}} \quad [77]$$

here q_l and A_{elec} are the flow rate and cross-section area of the flow channel.

Zero fluxes are specified at $x = x_3$,

$$\mathbf{N}_{l,j} = 0 \quad [78]$$

for $j = H^+$ in the anode electrode, $j = CO_2(l)$, OH^-, HCO_3^-, and CO_3^{2-} in the cathode electrode, respectively, and

$$\begin{aligned} -\mathbf{N}_{l,\mathrm{OH^-}}(x = x_3^-) &= \mathbf{N}_{l,\mathrm{H^+}}(x = x_3^+) = \mathbf{N}_{\mathrm{w,catalyst}} \\ \mathbf{N}_{l,\mathrm{K^+}}(x = x_3^-) &= \frac{\mathbf{i}_l}{F} - \mathbf{N}_{l,\mathrm{OH^-}}(x = x_3^-) \\ \mathbf{N}_{l,\mathrm{K^+}}(x = x_3^+) &= \frac{\mathbf{i}_l}{F} - \mathbf{N}_{l,\mathrm{H^+}}(x = x_3^+) \end{aligned} \quad [79]$$

where the flux of K^+ is calculated from electroneutrality.

For liquid phase transport, the initial ion concentrations in the corresponding electrolyte of anode or cathode electrode are,

$$c_j = c_j^0 \quad [80]$$

For Darcy's law in the gas or liquid phase, the initial values and the boundary conditions are specified as the corresponding inlet pressure, respectively.

$$p = p|_{x=x_1} = p|_{x=x_5} = p^0 \quad [81]$$

The boundary conditions for charge transport are set as follows.

There are no electrons crossing the ACL|AEL and CEL|CCL interfaces ($x = x_2$ and $x = x_4$),

$$\mathbf{i}_\mathrm{s}|_{x=x_2} = \mathbf{i}_\mathrm{s}|_{x=x_4} = 0 \quad [82]$$

Similarly, no electrolyte current density is applied at the anode channel|ACL and CCL|cathode channel interfaces ($x = x_1$ and $x = x_5$),

$$\mathbf{i}_l|_{x=x_1} = \mathbf{i}_l|_{x=x_5} = 0 \quad [83]$$

Electric zero-potential reference is set at the anode channel|ACL interface,

$$\phi_s|_{x=x_1} = 0 \quad [84]$$

and an electric potential is applied at the CCL|cathode channel interface,

$$\phi_\mathrm{s}|_{x=x_5} = \phi_\mathrm{s}^0 - a_3 \times i_{\mathrm{total}} \quad [85]$$

where ϕ_s^0 is the applied potential, i_{total} is the total current density through the cell, a_3 is a fitting parameter representing the Ohmic resistance which is not included in the model.

Donnan equilibrium conditions are applied at the ACL|AEL and CEL|CCL interfaces ($x = x_2$ and $x = x_4$),

$$\phi_l - \phi_m = -\frac{RT}{z_i F} \ln\left(\frac{c_{l,i}}{c_{m,i}}\right) \quad [86]$$

where ϕ_m is the potential in the membrane, $c_{l,i}$ and $c_{m,i}$ are the concentration of species i in electrolyte and membrane, respectively.

There is also an electric potential drop at the AEL|CEL interface ($x = x_3$) due to the differences in ion concentrations in the AEL and CEL.[25,37] A constant voltage drop, $\Delta\phi_l$, is applied here,

$$\phi_l|_{x=x_3^+} = \phi_l|_{x=x_3^-} - \Delta\phi_l \quad [87]$$

The electrolyte potential at $x = x_1$ is set to zero,

$$\phi_l|_{x=x_1} = 0 \quad [88]$$

The performance of the bicarbonate CO_2 electrolyzer is characterized by its CO Faradaic efficiency and CO yield which are calculated by

$$FE_{\mathrm{CO}} = \frac{i_{\mathrm{CO}}}{i_{\mathrm{total}}} = \frac{i_{\mathrm{CO}}}{i_{\mathrm{CO}} + i_{\mathrm{H_2}}} \quad [89]$$

and

$$\mathrm{CO\ yield} = \frac{c_{\mathrm{CO,outlet}}}{c_{\mathrm{CO_2,outlet}} + c_{\mathrm{CO,outlet}}} \quad [90]$$

here i_{CO} and $i_{\mathrm{H_2}}$ are the partial current densities for COER and HER respectively, $c_{\mathrm{CO_2,outlet}}$ and $c_{\mathrm{CO,outlet}}$ are the concentrations of CO_2 and CO at the outlet of the cathode electrode.

Numerical methods.—The model equations formulated above were solved using COMSOL Multiphysics software and the built-in Physics modules, i.e., Tertiary Current Distribution—Nernst Plank, Darcy's Law, and Transport of Concentrated Species. A fixed 250-element mesh was applied in both ACL and CCL domains and a predefined mesh with a distribution of 25 elements, 20 element ratio, and a linear growth rate was used in both AEL and CEL domains, and the mesh was then refined by a factor of 5. The default MUMPS solver was used with a relative tolerance of 0.001. An auxiliary sweep of the applied cathode potential (φ_s^0) from −2.75 V to −4.85 V with an increment step of 0.0005 was employed to simulate the required range of operating current densities.

Results and Discussion

Model validation.—The model was validated using the experimental data of FE_{CO}, CO yield, and polarization curves published in Ref. 38. It is worth noting that we assumed the proton flux from the catalyzed water splitting reaction at the AEL|CEL interface is proportional to the total cell current density in our cathode model.[31] In the current work, we refined this relationship and proposed a quadratic dependence of the flux on the electrolyte current density as given by Eq. 70. The model also considers the potential loss due to the internal resistance in the cell by introducing an additional term in the boundary condition of the applied electric potential at the cathode side (Eq. 85). The estimations of parameters are: $a_1 = 0.73$, $a_2 = -3e-5\mathrm{m^2A^{-1}}$ for the catalyzed water splitting reaction. At present, commercial BPMs have a typical area-specific

Table III. Parameters for model base-case simulation.

Parameter	Value	Unit	References
Operating Conditions			
T	293.15	K	—
p^0	1	atm	—
q_l	80	mL min^{-1}	12
ϕ_s^0	–2.75 to –4.85	V	
Geometry			
A_{elec}	7.5×10^{-6}	m^2	31
L_{elec}	0.02	m	31
ACL/CCL properties			
L_{ACL}, L_{CCL}	250	μm	31
a_v^0	1×10^5	m^{-1}	40
s_{ACL}, s_{CCL}	0.8	—	31
ε_{ACL}, ε_{CCL}	0.8	—	41
r_{ACL}, r_{CCL}	5	μm	41
$\kappa^0_{sat,ACL}$, $\kappa^0_{sat,CCL}$	8×10^{-16}	m^2	18
$\sigma_{s,ACL}$, $\sigma_{s,CCL}$	100	S cm^{-1}	18
AEL/CEL properties			
L_{AEL}, L_{CEL}	75	μm	41
IEC	1.99	mmol g^{-1}	31
ε_{mem}	0.39	—	42
ρ_m	1	g mL^{-1}	22
$\lambda_{H^+=0}$	6	—	22
$\lambda_{H^+=1}$	9	—	22
Homogeneous Reactions			
k_1	3.71×10^{-2}	s^{-1}	35
K_1	$10^{-6.37}$	M	35
k_2	59.44	s^{-1}	35
K_2	$10^{-10.32}$	M	35
k_3	2.23×10^3, 6.91×10^3	L mol^{-1} s^{-1}	35, 39
k_4	6.0×10^9	L mol^{-1} s^{-1}	35
Water splitting reactions			
a_1	0.73	—	estimated
a_2	-3×10^{-5}	m^2 A^{-1}	estimated
A	0.09636	K^2 m V^{-1}	24
k_{-w}	1.3×10^{11}	M^{-1} s^{-1}	30
K_w	10^{-14}	M^2	24
ε^{rel}	78	—	24
Electrochemical Reactions			
$U^0_{CO_2RR}$	–0.11	V	17
i_{0,CO_2RR}	1.1×10^9	mA cm^{-2}	17
α_{c,CO_2RR}	1	—	17
$c^{ref}_{CO_2(aq)}$	1	M	17
U^0_{HER}	0	V	17
$i^A_{0,HER}$	9.79×10^{-4}	mA cm^{-2}	17
$i^B_{0,HER}$	1.16×10^{-6}	mA cm^{-2}	17
$\alpha^A_{c,HER}$	0.27	—	17
$\alpha^B_{c,HER}$	0.33	—	31
$c^{ref}_{H^+}$	1	M	17
U^0_{OER}	1.23	V	18
A^A_{OER}	9.4×10^{-7}	mA cm^{-2}	18
A^B_{OER}	1.23×10^{-4}	mA cm^{-2}	18
α_{OER}	1	—	18
$c^{ref}_{OH^-}$	1	M	18
Liquid phase transport			
$D_{H^+,w}$	9.31×10^{-5}	cm^2 s^{-1}	19
$D_{K^+,w}$	1.96×10^{-5}	cm^2 s^{-1}	19
$D_{OH^-,w}$	4.95×10^{-5}	cm^2 s^{-1}	19
$D_{HCO_3^-}$	1.19×10^{-5}	cm^2 s^{-1}	19
$D_{CO_3^{2-}}$	0.80×10^{-5}	cm^2 s^{-1}	19

Table III. (Continued).

Parameter	Value	Unit	References
$D_{CO_2(aq)}$	1.66×10^{-5}	$cm^2\ s^{-1}$	19
Gas phase transport			
$D_{H_2,CO}$	0.743	$cm^2\ s^{-1}$	18
D_{H_2,N_2}	0.779	$cm^2\ s^{-1}$	18
D_{H_2,CO_2}	0.646	$cm^2\ s^{-1}$	18
D_{CO,N_2}	0.202	$cm^2\ s^{-1}$	18
D_{CO,CO_2}	0.152	$cm^2\ s^{-1}$	18
D_{N_2,CO_2}	0.165	$cm^2\ s^{-1}$	18
D_{N_2,O_2}	0.219	$cm^2\ s^{-1}$	18
Bulk concentrations in the liquid phase of the cathode			
$c^0_{H^+}$	$10^{-8.5}$	M	31
$c^0_{K^+}$	3	M	31
$c^0_{OH^-}$	$10^{-5.5}$	M	31
$c^0_{HCO_3^-}$	3	M	31
$c^0_{CO_3^{2-}}$	0	M	31
$c^0_{CO_2(aq)}$	0.008	M	31
Bulk concentrations in the liquid phase of anode (Calculated from 1 M KOH solution[13])			
$c^0_{H^+}$	1.2550×10^{-14}	M	
$c^0_{K^+}$	0.79682	M	
$c^0_{OH^-}$	0.79682	M	
c^0_{KOH}	0.20318	M	
Bulk concentrations in the gas phase of the cathode			
$\omega^0_{H_2}$	0.0005	—	13
ω^0_{CO}	0.0005	—	13
$\omega^0_{CO_2}$	0.002	—	13
$\omega^0_{N_2}$	0.997	—	13
Bulk concentrations in the gas phase of the anode			
$\omega^0_{O_2}$	0.233	—	13
$\omega^0_{N_2}$	0.767	—	13
Other parameters			
a_3	4.2	$\Omega\ m^2$	estimated
$\Delta\phi_l$	1.5	V	estimated

resistance of 3∼10 Ωcm^2,[2] and in our case, it is estimated as $a_3 = 4.2\ \Omega cm^2$. All the parameters used in the base-case simulation scenario are listed in Table III. As pointed out by Borhani et al.,[39] the reported value for k_3 ranges from 2×10^3 to $5 \times 10^5\ L\ mol^{-1}\ s^{-1}$ in the temperature range of 293–373 K for dilute and low concentration of potassium carbonate solutions. A value of $5.91 \times 10^5\ L\ mol^{-1}\ s^{-1}$ is obtained based on Astarita's formula in Ref. 39 and listed in Table III for reference. $k_3 = 2.23 \times 10^3\ L\ mol^{-1}\ s^{-1}$ from Ref. 35 is used in the current simulation. The values of a_1, a_2, and a_3 are all fitted by using experimental data of FE_{CO}, CO yield, and polarization curve published in Ref. 38.

The comparisons of model fitting and experimental results of FE_{CO}, CO yield, and polarization curve are plotted in Figs. 2a–2c, respectively. The operating current density range is from $20\ mAcm^{-2}$ to $300\ mAcm^{-2}$. It can be seen that the developed MEA model can simulate the FE_{CO} and CO yield remarkably well in the whole current density range. The calculated polarization curve is highly consistent with the experimental data at low current densities, however, there is a large discrepancy at the high current density point of $300\ mAcm^{-2}$. The sharp decrease in potential at the higher current densities is due to bubbles forming on both sides, blocking the electrodes and limiting access of reactants and this mass transport limitation is not considered in in the current model.

Potential profiles.—The electrolyte and electric potential distributions over the thickness of the MEA at different applied cathode electric potentials are shown in Fig. 3. The sudden changes in ion concentrations through the interfaces of ACL|AEL and CEL|CCL cause non-zero Donann potentials which are described by the Donnan equilibrium conditions given by Eq. 86. For simplicity, the potential drop at the interface of AEL|CEL is taken as a constant in this case: $\Delta\phi_l = 1.5$ V. Consistent with the behavior depicted in Refs. 22, 25, the electrolyte potential decreases in the ACL from left to the interface of ACL|AEL, then jumps to a higher level in the AEL due to Donnan potential, then drops significantly in the CEL through the interface of AEL|CEL because of Donnan potential and internal resistance, and finally jumps slightly in the CCL through the interface of CEL|CCL due to Donnan potential again. Decreasing the applied electric potential will enlarge the drops both in the electrolyte and electric potentials of the anode and cathode electrodes, as shown in Figs. 3a and 3b, respectively. It is noted that the anode electric potential profile is nearly identical for the given three applied potentials compared to the cathode potential profiles, indicating that the electric potential loss in the anode is negligible compared to the loss in the cathode electrode. The electric potential at the anode channel|ACL interface is grounded (Eq. 84) and Ohmic loss in the ACL is small due to its high electric conductivity. When the applied electric potential at the CCL|cathode channel increases

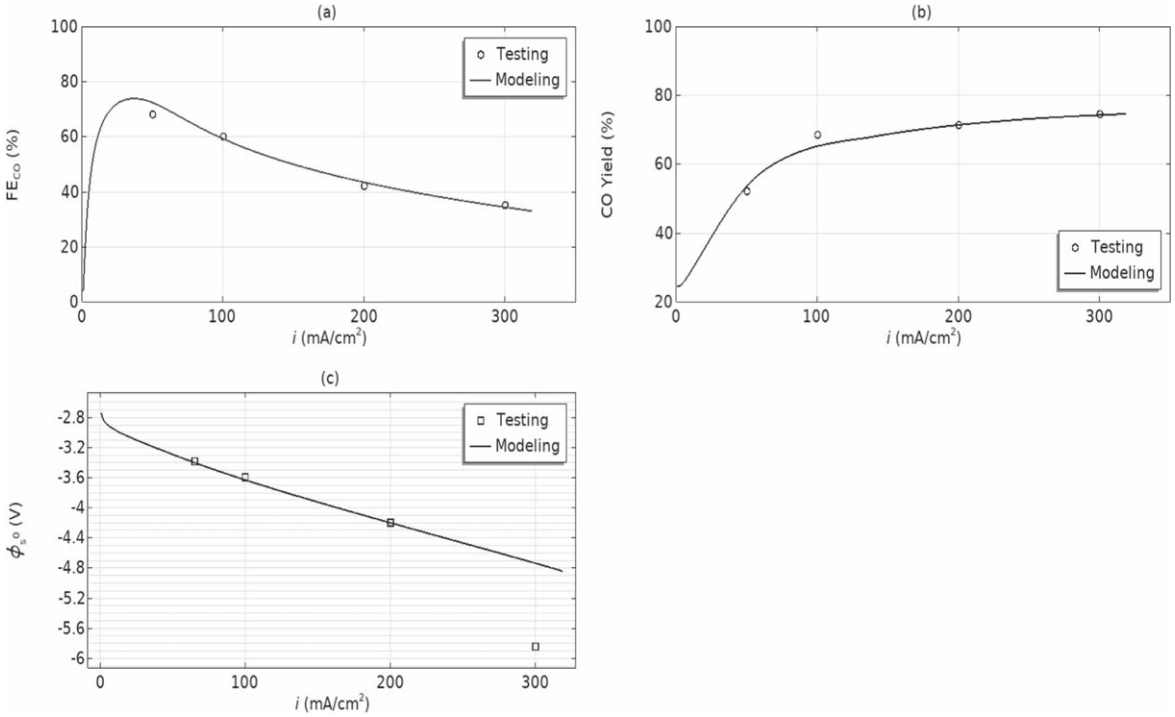

Figure 2. Comparisons of modeling and measured results for BPM carbonate CO2 electrolyzers.(a) FE_{CO}, (b) CO yields, and (c) Polarization curve

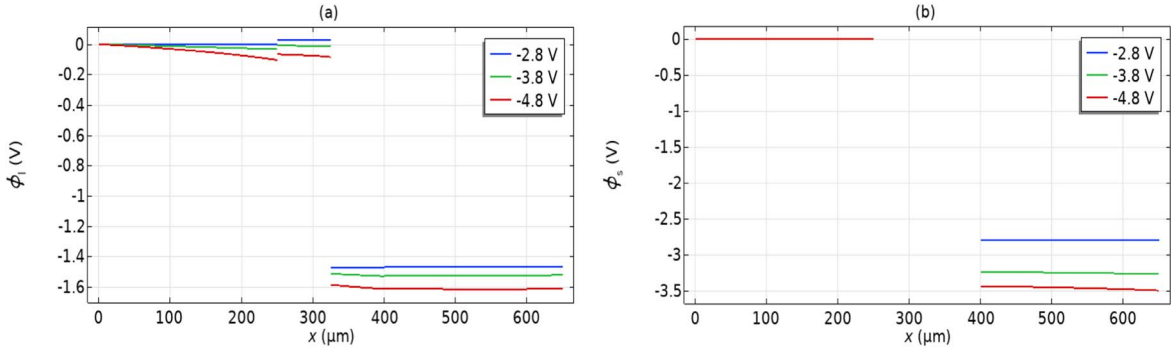

Figure 3. Simulated electrolyte and electric potential distributions at $\phi_s^0 = -2.8$ V, -3.8 V, and $-$ 4.8 V. (ACL: 0 $\sim$ 250 μm; AEL: 250 μm $\sim$ 325 μm; CEL: 325 μm $\sim$ 400 μm; CCL: 400 μm $\sim$ 650 μm).

from -2.8 V to -4.8 V, almost all the increases are soaked up in the cathode reaction overpotential, therefore, the electric potential profiles in the ACL barely change.

Gas phase species profiles.—The mass fractions of gaseous species in the cathode and anode electrodes are plotted in Fig. 4. At high applied potential (corresponding to high current density), more H_2, CO, and O_2 are produced so their mass fraction profiles are higher at a lower applied potential, as shown in Figs. 4a, 4c, and 4d, respectively. Meanwhile, a higher current density results in more CO_2(aq) consumed in the COER and requires more CO_2(g) transfers to CO_2(aq), therefore, less CO_2(g) in the cathode gaseous phase, as shown in Fig. 4b.

CO_2(aq) concentration, CO_2(g) pressure, CO_2 phase change, CO production, and pH.—Figure 5 shows the spatial distributions of liquid phase CO_2 concentrations, gas phase CO_2 partial pressure, rate of CO_2 phase transition, and rate of CO production for the three applied electric potentials $\phi_s^0 = -2.8$ V, -3.8 V, and $-$ 4.8 V. The corresponding pH profiles are given in Fig. 6, where a highly acidic thin layer (<300 nm) in the CEL close to the AEL|CEL interface exists mainly due to the fast buffer reaction Eq. 7. In the CEL, the concentrations of both proton and bicarbonate ions are higher close to the AEL|CEL interface than the concentrations close to the CEL|CCL interface, therefore, the CO_2(aq) concentration varies accordingly based on the CO_2 hydrolysis reactions 6 and 8. Higher applied electric potentials (higher current densities) correspond to higher proton fluxes from the water splitting reaction at the AEL|CEL interface, and lead to higher acidity in this thin layer (shown inset within Fig. 6), and therefore, produce higher CO_2(aq) in the CEL as shown on the left side of Fig. 5. As demonstrated by Zhu et al.[43] for the formic acid oxidation reaction, pH has a significant effect on electrocatalysis and needs to be further investigated. CO_2(aq) concentration drops sharply across the CEL|CCL interface from the CEL to the CCL due to both the highest phase change rate of CO_2 from liquid to gas as shown in Fig. 5c and the highest conversion rate of CO_2(aq) to CO as shown in Fig. 5d in this region. In the CCL, higher applied electric potentials result in higher CO_2(aq) consumption, and therefore, result in lower CO_2(aq) concentration profiles on the right hand side of Fig. 5 and lower CO_2 gas partial pressure in Fig. 5b.

It is noted from Fig. 5c that, at low applied electric potential ($\phi_s^0 = -2.8$ V), the rate of CO_2 phase transition, $R_{PT,CO_2} < 0$, indicating CO_2(aq) is adequate for the CO_2RR and extra CO_2

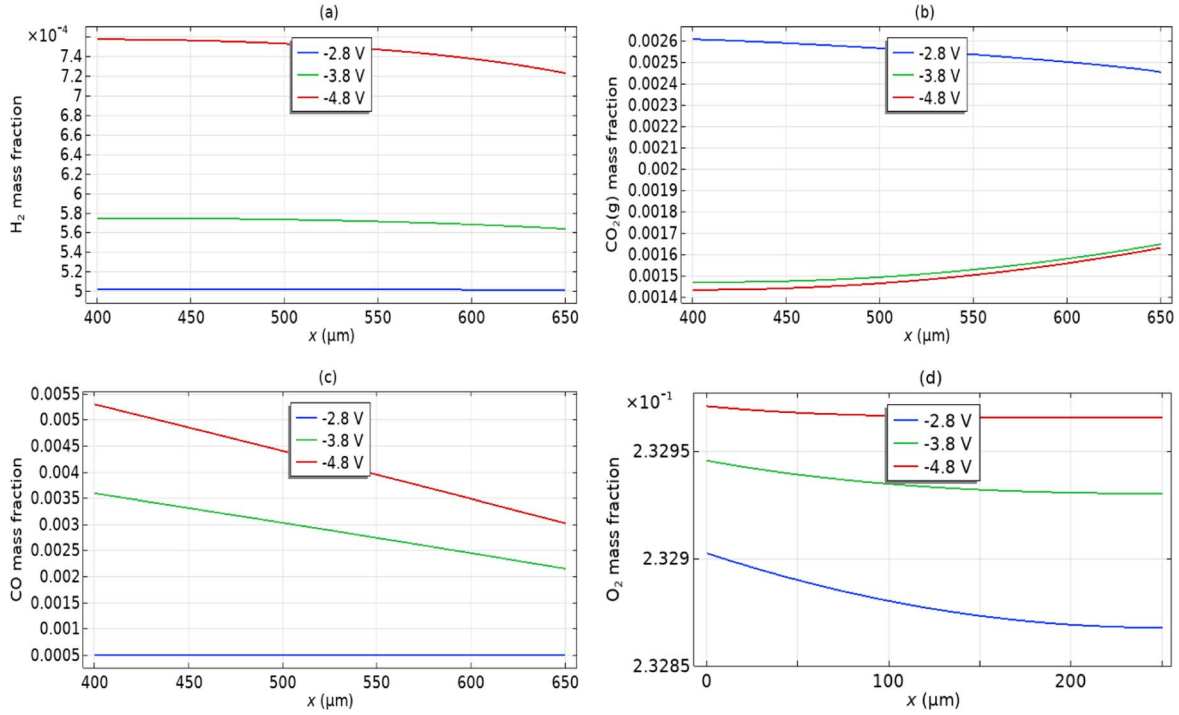

Figure 4. Mass fraction profiles of gaseous species in the cathode and anode electrodes. (ACL: 0 $\sim$ 250 μm; CCL: 400 μm $\sim$ 650 μm).

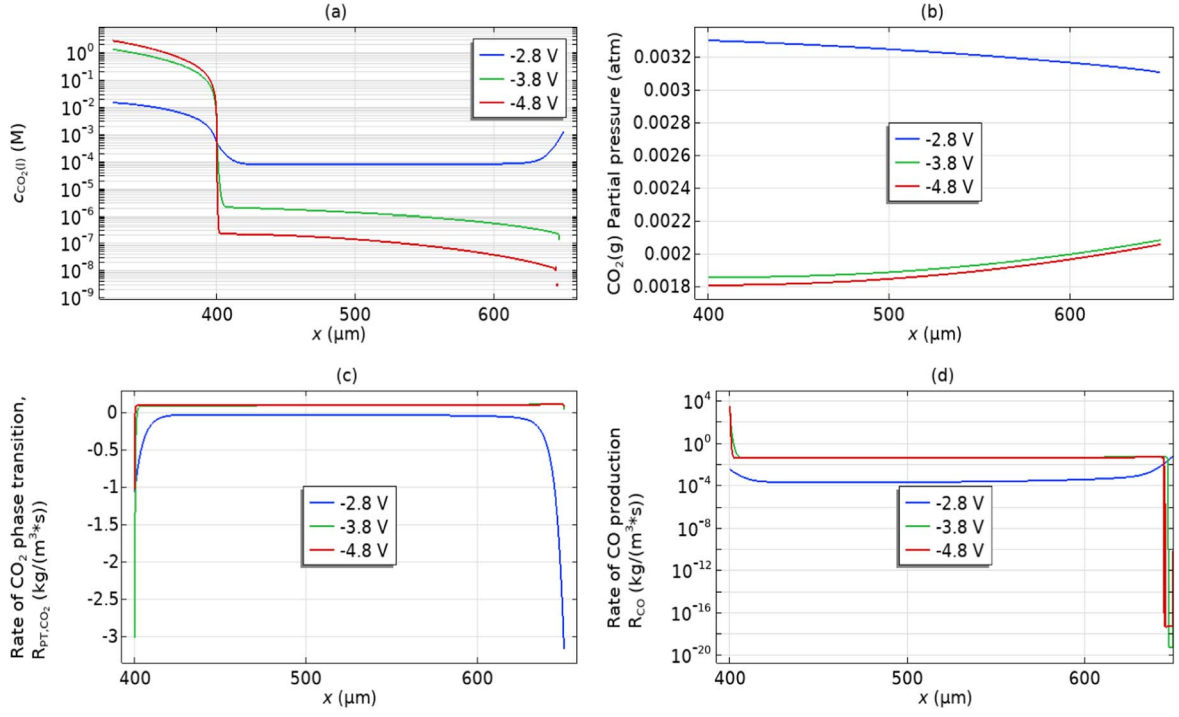

Figure 5. CO_2(aq) concentration, CO_2(g) partial pressure, phase change rate, and current densities in the cathode electrode. (CEL: 325 μm $\sim$ 400 μm; CCL: 400 μm $\sim$ 650 μm).

transfers from the liquid phase to the gas phase. However, when higher electric potentials are applied, the phase change of CO_2 from liquid to gas ($R_{PT,CO_2} < 0$) only occurs in the CCL close to the CEL|CCL interface. For the rest of the CCL, the CO_2 phase changes from gas to liquid ($R_{PT,CO_2} > 0$) due to higher CO_2(aq) consumption of the CO_2RR.

The rates of CO production in the CCL for the three applied electric potentials are plotted in Fig. 5d. The highest CO production rate is found inside the CCL next to the CEL|CCL interface due to the highest CO_2(aq) concentration at this interface, as shown in Fig. 5a.

Parametric study.— *Effects of water splitting reaction.*— Simulation results show that the Wien effect of the non-catalyzed water splitting reaction on the electrolyzer performance within the electrode domain is negligible due to a weak electric field. For the catalyzed water

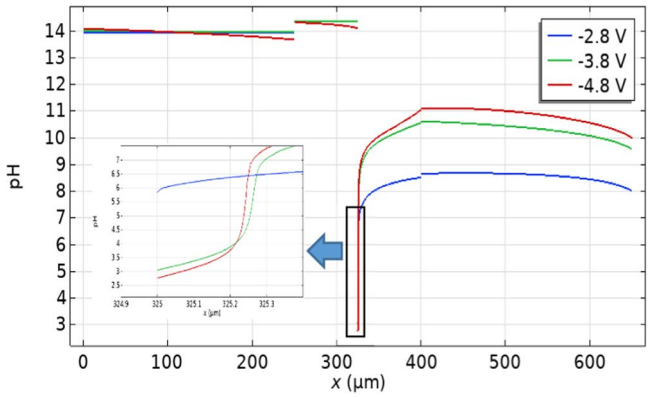

Figure 6. pH distributions through the MEA at different applied electric potentials. (ACL: 0 ∼ 250 μm; AEL: 250 μm ∼ 325 μm; CEL: 325 μm ∼ 400 μm; CCL: 400 μm ∼ 650 μm).

splitting reaction at the AEL|CEL interface of the BPM, the maximum electric field across the interface can be roughly estimated by (Eq. 38 in Ref. 30): $E_m \approx -\Delta\phi_l/(2\lambda_{SCR}) = 0.75 \times 10^9\ \mathrm{Vm^{-1}}$, here $\Delta\phi_l = 1.5$ V is the potential drop across the AEL|CEL interface, $\lambda_{SCR} = 1$ nm is the thickness of the space charge region in the AEL|CEL interfacial region. Studies[30,44] show that the electric field across the AEL|CEL interface of a BPM is typically in the order of $10^9\ \mathrm{V\ m^{-1}}$, and k_d/k_d^0 is in the order of 10^5. The enhancement of the electric field across the AEL|CEL interface on the catalyzed water splitting reaction is essential for the BPM-based bicarbonate CO_2 electrolyzers to obtain the demonstrated performance as shown in Fig. 2. However, the abrupt increase/decrease in the electric field strength across the AEL|CEL interface of the BPM makes it extremely difficult to find a numerical solution for the MEA model. Therefore, for the boundary condition of the protons or hydroxide ion flux from the catalyzed water splitting reaction, we proposed a quadratic dependence on the current density of the electrolyte phase (Eq. 70). The effects of the electric field across the AEL|CEL interface of the BPM can be indirectly investigated by adjusting the parameter a_1 or a_2.

To check how the catalyzed water splitting reaction affects the electrolyzers' performance, three different a_1 values, $a_1 =$ 0.63, 0.73 and 0.83, are used to conduct the simulations and the results are presented in Fig. 7. A larger a_1 value means a higher proton flux from the catalyzed water splitting reaction at the AEL|CEL interface going into the CEL that provides higher acidity in the acidic thin layer of the CEL, as shown in Fig. 7c. The higher acidity will produce more CO_2 based on the homogeneous reactions 6 and 8, thereby accelerate the CO_2ER reaction and generate more CO. Therefore, a larger a_1 value leads to higher FE_{CO} and higher CO yield as shown in Figs. a and 7b, respectively. It is worth noting that smaller a_1 values will also significantly reduce the maximum attainable current density of the electrolyzer because of higher bubble formation rates on both sides, resulting in the mass transport limitations previously discussed.

Effects of the membrane porosity.—The effects of the membrane porosity on electrolyzers' performance are shown in Fig. 8. On the one hand, increasing the membrane porosity will increase the available liquid volume to the membrane and dilute the proton concentration, and therefore, reduce the CO_2 generation in the CEL and lower the FE_{CO} and CO yield of the electrolyzer. On the other hand, a larger porosity will allow more catholyte to participate in the homogeneous reaction of the CO_2 production and then improve the performance. Overall, the former mechanism is found to dominate the latter one and so both the FE_{CO} and CO yield of the electrolyzer have been marginally reduced.

Effects of the catalyst layer porosity.—Figure 9 compares the performance resulting from variations in the catalyst layer porosity. Both the FE_{CO} and CO yield are improved when the catalyst porosity is increased from 0.7 to 0.9 because larger porosity is beneficial to the transport of both CO_2(aq) from the CEL into the CCL and CO out of the CCL.

Note: The specific surface area is determined by the composition and the pore network/microstructure of the electrode. The active

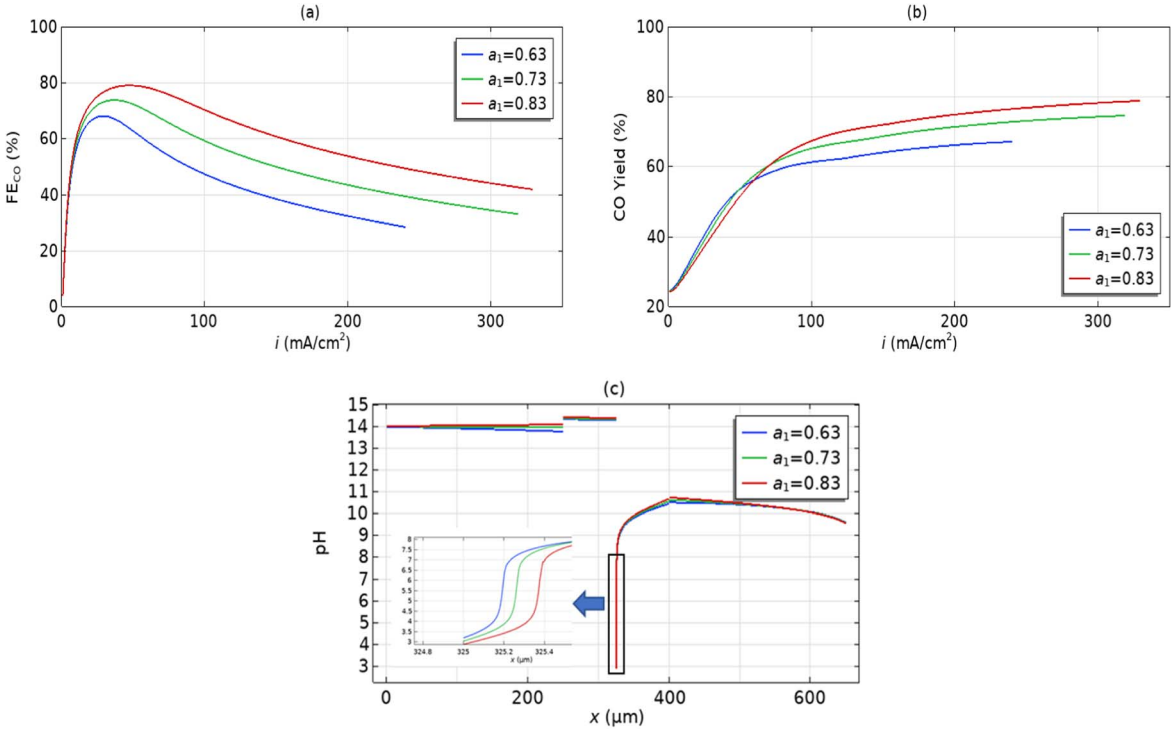

Figure 7. Effects of water splitting reaction on the electrolyzers' performance and pH.

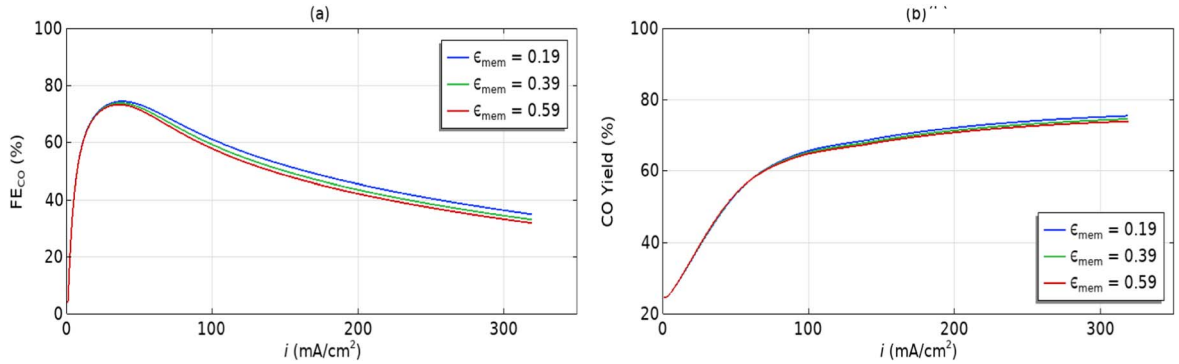

Figure 8. Effects of the membrane porosity on the electrolyzers' performance.

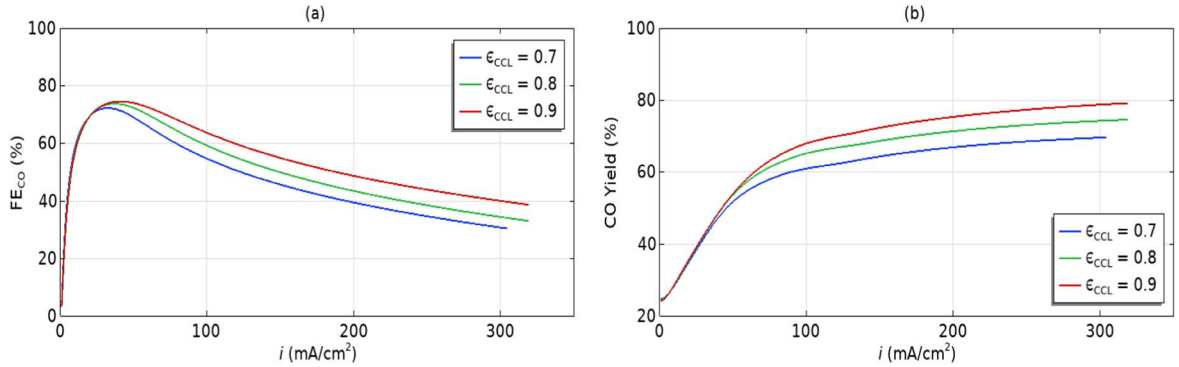

Figure 9. Effects of the catalyst layer porosity on the electrolyzers' performance.

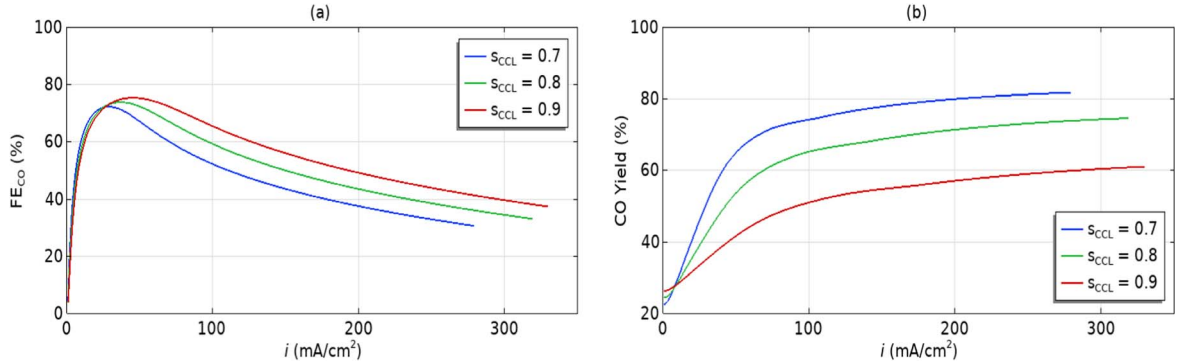

Figure 10. Effects of the electrolyte saturation in the cathode catalyst layer on the electrolyzers' performance.

specific surface area of an electrode changes with its porosity. This dependence of the active surface area on porosity is too complex and is not considered in the current work, and will be studied in the future.

Effects of the electrolyte saturation.—Experiment[13] shows that CO_2 bubbles out of the cathode indicating that the cathode is not fully flooded during the electrolysis process. The CEL of the BPM is fully flooded where Bicarbonate ions are converted to aqueous CO_2 when reacting with protons coming from the catalyzed water splitting at the interface of the BPM. Some of the aqueous CO_2 is transitioned into gaseous CO_2 to form CO_2 bubbles at the EL|CCL interface due to capillary pressure. The triple-phase boundary/interface (CO_2 bubbles, liquid electrolyte, and Ag catalyst) exists in the CCL, hence the electrode is not fully flooded. Assuming the electrolyte saturation $s < 1$, only s portion of the pore domain is used to provide water and bicarbonate fluxes to the reaction zone, $(1 - s)$ portion is used for gas phase transport. The gas phase transport Eq. 11 is solved using the Transport of Concentrated Species Interface (tcl) module in the COMSOL software. The liquid phase transport Eq. 44 is solved using the Tertiary Current distribution-Nernst Planck Interface (tcd) in the COMSOL software. These two sets of equations are coupled by the related source terms R_j.

It is demonstrated that electrode wettability plays an important role in the electrochemical reduction of CO_2.[45] The electrolyte saturation depends highly on the electrode wettability. The COER reaction takes place in the liquid phase of the CCL and converts CO_2(aq) into CO. CO gas, together with H_2 from the HER and other gaseous species (CO_2(g) and N_2), transports out through the void space of the CCL. Increasing the electrolyte saturation in the CCL will accelerate the CO_2(aq) conversion of the COER by enlarging its reaction surface area and reaction volume (Eq. 40). However, increasing the electrolyte saturation will reduce the void space in the CCL and slow down the phase transfer of CO_2(g) into CO_2(aq) (Eq. 39), therefore, increase the CO_2(g) concentration at the outlet.

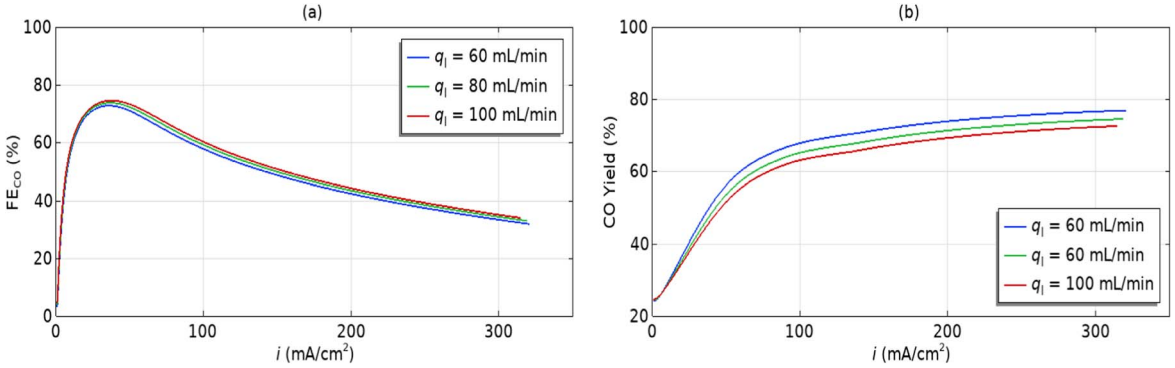

Figure 11. Effects of the flow rate on the electrolyzers' performance.

As expected, increasing the electrolyte saturation in the CCL will improve the FE_{CO} but worsen the CO yield, as shown in Figs. a and 10b respectively.

Effects of the flow rate.—The calculated FE_{CO} and CO yield of the electrolyzer under different flow rates are plotted in Fig. 11 as functions of current density. The FE_{CO} is slightly improved with the flow rate increase because a higher flow rate will enhance the bicarbonate transport in the cathode electrode, benefit the CO_2(aq) generation from the homogeneous reactions 6 and 8, and increase the phase transfer from CO_2(g) to CO_2(aq). Therefore, the higher CO_2(aq) concentration leads to better CO_2RR and then better FE_{CO}, as shown in Fig. 11a while a higher CO_2(g) concentration results in lower CO yield as shown in Fig. 11b.

Modeling simulations are also performed for the polarization curves and it is found that all the above parameters have negligible effects on the corresponding polarization curves.

Conclusions

This study reports a 1-D mathematical model for the MEA of a bicarbonate CO_2 electrolyzer with a BPM design. The model incorporates catalyzed water splitting at the AEL|CEL interface and non-catalyzed water electrolysis through the model domain with the Wien effect. Furthermore, the model captures the discontinuities in the potential and species concentrations at ACL|AEL, AEL|CEL, and CEL|CCL interfaces.

The model can simulate the FE_{CO}, CO yield, and polarization curve with good agreement with available experimental data when a quadratic dependence on the electrolyte current density is used for the proton flux from the catalyzed water splitting reaction at the AEL|CEL interface. The modeling results demonstrate that there is a highly acidic thin layer (<300 nm) in the CEL close to the AEL|CEL interface where CO_2 is rapidly produced. Among the parameters used in the parametric study, the model simulations suggest that the catalyzed water splitting reaction and the aqueous electrolyte saturation in the CCL have the highest impacts on the FE_{CO} and CO yield of the electrolyzer, indicating that the catalyst development for water splitting reaction and the hydrophobicity treatment for the cathode catalyst layer are critical for performance improvement of bicarbonate electrolyzers.

A more complicated cell model including ion species crossover and flow channels is required to capture the mass transport limitation phenomenon. In addition, the quadratic dependence for the proton flux on the electrolyte current density for the catalyzed water splitting reaction at the AEL|CEL interface needs to be directly validated by experiments.

ORCID

Datong Song https://orcid.org/0000-0003-0339-6680

References

1. W. Zhang, Y. Hu, L. Ma, G. Zhu, Y. Wang, X. Xue, R. Chen, S. Yang, and Z. Jin, "Progress and perspective of electrocatalytic CO_2 reduction for renewable carbonaceous fuels and chemicals." *Adv. Sci.*, **5**, 1700275 (2018).
2. M. A. Blommaert, D. Aili, R. A. Tufa, Q. Li, W. A. Smith, and D. A. Vermaas, "Insights and challenges for applying bipolar membranes in advanced electrochemical energy systems." *ACS Energy Lett.*, **6**, 2539 (2021).
3. Y. Pei, H. Zhong, and F. Jin, "A brief review of electrocatalytic reduction of CO_2—Materials, reaction conditions, and devices." *Energy Science & Engineering*, **9**, 1012 (2021).
4. M. Jouny, W. Luc, and F. Jiao, "General techno-economic analysis of CO_2 electrolysis systems." *Ind. Eng. Chem. Res.*, **57**, 2165 (2018).
5. S. Verma, S. Lu, and P. A. Kenis, "Co-electrolysis of CO_2 and glycerol as a pathway to carbon chemicals with improved technoeconomics due to low electricity consumption." *Nat. Energy*, **4**, 466 (2019).
6. A. Badgett, M. Ruth, A. Crow, Y. Chen, L. Hu, L. Tao, W. Smith, K. C. Neyerlin, and R. Cortright, "An economic analysis of the role of materials, system engineering, and performance in electrochemical carbon dioxide conversion to formate." *Journal of Cleaner Production*, **351**, 131564 (2022).
7. Z. Zhang, E. W. Lees, S. Ren, B. A. W. Mowbray, A. Huang, and C. P. Berlinguette, "Conversion of reactive carbon solutions into CO at low voltage and high carbon efficiency." *ACS Central Science*, **8**, 749 (2022).
8. C. Delacourt, P. L. Ridgway, J. B. Kerr, and J. Newman, "Design of an electrochemical cell making syngas (CO + H_2) from CO_2 and H_2O reduction at room temperature." *J. Electrochem. Soc.*, **155**, B42 (2008).
9. D. Corral et al., "Advanced manufacturing for electrosynthesis of fuels and chemicals from CO_2." *Energy Environ. Sci.*, **14**, 3064 (2021).
10. C.-T. Dinh et al., "CO_2 electroreduction to ethylene via hydroxide-mediated copper catalysis at an abrupt interface." *Science*, **360**, 783 (2018).
11. F. P. Gd Arquer et al., "CO_2 electrolysis to multicarbon products at activities greater than 1 A cm^{-2}." *Science*, **367**, 661 (2020).
12. E. W. Lees, M. Goldman, A. G. Fink, D. J. Dvorak, D. A. Salvatore, Z. Zhang, N. W. X. Loo, and C. P. Berlinguette, "Electrodes designed for converting bicarbonate into CO." *ACS Energy Lett.*, **5**, 2165 (2020).
13. T. Li, E. W. Lees, M. Goldman, D. A. Salvatore, D. M. Weekes, and C. P. Berlinguette, "Electrolytic conversion of bicarbonate into CO in a flow cell." *Joule*, **3**, 1487 (2019).
14. J. C. Bui, E. W. Lees, L. M. Pant, I. V. Zenyuk, A. T. Bell, and A. Z. Weber, "Continuum modeling of porous electrodes for electrochemical synthesis." *Chem. Rev.*, **122**, 11022 (2022).
15. C. Delacourt, P. L. Ridgway, and J. Newman, "Mathematical modeling of CO_2 reduction to CO in aqueous electrolytes i. kinetic study on planar silver and gold electrodes." *J. Electrochem. Soc.*, **157**, B1902 (2010).
16. C. Delacourt and J. Newman, "Mathematical modeling of CO_2 reduction to CO in aqueous electrolytes II. study of an electrolysis cell making syngas (CO + H_2) from CO_2 and H_2O reduction at room temperature." *J. Electrochem. Soc.*, **157**, B1911 (2010).
17. L.-C. Weng, A. T. Bell, and A. Z. Weber, "Modeling gas-diffusion electrodes for CO_2 reduction." *Phys. Chem. Chem. Phys.*, **20**, 16973 (2018).
18. L.-C. Weng, A. T. Bell, and A. Z. Weber, "Towards membrane-electrode assembly systems for CO_2 reduction: a modeling study." *Energy Environ. Sci.*, **12**, 1950 (2019).
19. L.-C. Weng, A. T. Bell, and A. Z. Weber, "A systematic analysis of Cu-based membrane electrode assemblies for CO_2 reduction through multiphysics simulation." *Energy Environ. Sci.*, **13**, 3592 (2020).
20. C. McCallum, C. M. Gabardo, C. P. O'Brien, J. E. Edwards, J. Wicks, Y. Xu, E. H. Sargent, and D. Sinton, "Reducing the crossover of carbonate and liquid products during carbon dioxide electroreduction." *Cell Reports Physical Science*, **2**, 100522 (2021).
21. R. Parnamae, S. Mareev, V. Nikonenko, S. Melnikov, N. Sheldeshov, V. Zabolotskii, H. V. M. Hamelers, and M. Tedesco, "Bipolar membranes: a review on principles, latest developments, and applications." *J. Membr. Sci.*, **617**, 118538 (2021).
22. J. C. Bui, I. Digdaya, C. Xiang, A. T. Bell, and A. Z. Weber, "Understanding multi-ion transport mechanisms in bipolar membranes." *ACS Appl. Mater. Interfaces*, **12**, 52509 (2020).

23. J. C. Bui, K. R. M. Corpus, A. T. Bell, and A. Z. Weber, "On the nature of field-enhanced water dissociation in bipolar membranes." *J. Phys. Chem. C*, **125**, 24974 (2021).
24. R. Kodym, D. Snita, and K. Bouzek, "Mathematical modeling of electromembrane processes." *Current Trends and Future Developments on (Bio-) Membranes*, ed. A. Basile et al. (Elsevier, Amsterdam) p. 285 (2019).
25. D. A. Vermaas, S. Wiegman, T. Nagaki, and W. A. Smith, "Ion transport mechanisms in bipolar membranes for (photo) electrochemical water splitting." *Sustainable Energy & Fuels*, **2**, 2006 (2018).
26. J. A. Wrubel, Y. Chen, Z. Ma, and T. G. Deutsch, "Modeling water electrolysis in bipolar membranes." *J. Electrochem. Soc.*, **167**, 114502 (2020).
27. N. P. Craig, *Electrochemical Behavior of Bipolar Membranes* (University of California, Berkeley) (2013).
28. B. Mayerhofer, D. McLaughlin, T. Bohm, M. Hegelheimer, D. Seeberger, and S. Thiele, "Bipolar membrane electrode assemblies for water electrolysis." *ACS Appl. Energy Mater.*, **3**, 9635 (2020).
29. I. Miesiac and B. Rukowicz, "Bipolar membrane and water splitting in electro-dialysis." *Electrocatalysis*, **13**, 101 (2022).
30. S. A. Mareev, E. Evdochenko, M. Wessling, O. A. Kozaderova, S. I. Niftaliev, N. D. Pismenskaya, and V. V. Nikonenko, "A comprehensive mathematical model of water splitting in bipolar membranes: impact of the spatial distribution of fixed charges and catalyst at bipolar junction." *J. Membr. Sci.*, **603**, 118010 (2020).
31. E. W. Lees, J. C. Bui, D. Song, A. Z. Weber, and C. P. Berlinguette, "Continuum model to define the chemistry and mass transfer in a bicarbonate electrolyzer." *ACS Energy Lett.*, **7**, 834 (2022).
32. J. Cai, E. Griffin, V. H. Guarochico-Moreira, D. Barry, B. Xin, M. Yagmurcukardes, S. Zhang, A. K. Geim, F. M. Peeters, and M. Lozada-Hidalgo, "Wien effect in interfacial water dissociation through proton-permeable graphene electrodes." *Nat. Commun.*, **13**, 5776 (2022).
33. P. C. Carman, "Fluid flow through granular beds." *Chem. Eng. Res. Des.*, **75**, S32 (1997).
34. K. N. Grew and W. K. Chiu, "A dusty fluid model for predicting hydroxyl anion conductivity in alkaline anion exchange membranes." *J. Electrochem. Soc.*, **157**, B327 (2010).
35. K. G. Schulz, U. Riebesell, B. Rost, S. Thoms, and R. E. Zeebe, "Determination of the rate constants for the carbon dioxide to bicarbonate inter-conversion in pH-buffered seawater systems." *Mar. Chem.*, **100**, 53 (2006).
36. Z. Yan, L. Zhu, Y. C. Li, R. J. Wycisk, P. N. Pintauro, M. A. Hickner, and T. E. Mallouk, "The balance of electric field and interfacial catalysis in promoting water dissociation in bipolar membranes." *Energy Environ. Sci.*, **11**, 2235 (2018).
37. N. M. Vargas-Barbosa, G. M. Geise, M. A. Hickner, and T. E. Mallouk, "Assessing the utility of bipolar membranes for use in photoelectrochemical water-splitting cells." *ChemSusChem*, **7**, 3017 (2014).
38. Z. Zhang, Z. W. Lees, F. Habibzadeh, D. A. Salvatore, S. Ren, G. Simpson, D. Wheeler, A. Liu, and C. P. Berlinguette, "Porous metal electrodes enable efficient electrolysis of carbon capture solutions." *Energy Environ. Sci.*, **15**, 705 (2022).
39. T. N. G. Borhani, A. Azarpour, V. Akbari, S. R. W. Alwi, and Z. A. Manan, "CO_2 capture with potassium carbonate solutions: a state-of-the-art review." *Int. J. Greenhouse Gas Control*, **41**, 142 (2015).
40. Y. Chen, N. S. Lewis, and C. Xiang, "Modeling the performance of a flow-through gas diffusion electrode for electrochemical reduction of CO or CO_2." *J. Electrochem. Soc.*, **167**, 114503 (2020).
41. Z. Zhang, E. W. Lees, F. Habibzadeh, D. A. Salvatore, S. Ren, G. Simpson, D. Wheeler, A. Liu, and C. P. Berlinguette, (2021) 1–20, https://chemrxiv.org/engage/api-gateway/chemrxiv/assets/orp/resource/item/60c77673ee301c620bc7baa4/.
42. D. Joseph, J. Büsselmann, C. Harms, D. Henkensmeier, M. J. Larsen, A. Dyck, J. H. Jang, J. Kim, and S. W. Nam, "Porous nafion membranes." *J. Membr. Sci.*, **520**, 723 (2016).
43. X. Zhu, J. Huang, and M. Eikerling, "pH Effects in a model electrocatalytic reaction disentangled." *JACS Au*, **3**, 1052 (2023).
44. R. J. Martinez and J. Farrell, "Water splitting activity of oxygen-containing groups in graphene oxide catalyst in bipolar membranes." *Computational and Theoretical Chemistry*, **1164**, 112556 (2019).
45. M. Li, M. N. Idros, Y. Wu, T. Burdyny, S. Garg, X. S. Zhao, G. Wanga, and T. E. Rufford, "The role of electrode wettability in electrochemical reduction of carbon dioxide." *J. Mater. Chem. A*, **9**, 19369 (2021).